Acta Crystallographica Section F
Structural Biology and Crystallization Communications
ISSN 1744-3091

Structure of *Staphylococcus aureus* 5′-methylthioadenosine/*S*-adenosylhomocysteine nucleosidase

Karen K. W. Siu,[a,b] Jeffrey E. Lee,[a,b]‡ G. David Smith,[a] Cathy Horvatin-Mrakovcic[a] and P. Lynne Howell[a,b]*

[a]Program in Molecular Structure and Function, Research Institute, The Hospital for Sick Children, 555 University Avenue, Toronto, Ontario M5G 1X8, Canada, and [b]Department of Biochemistry, University of Toronto, Toronto, Ontario M5S 1A8, Canada

‡ Present address: Department of Immunology, The Scripps Research Institute, 10550 North Torrey Pines Road, La Jolla, CA 92037, USA.

Correspondence e-mail: howell@sickkids.ca

Received 4 January 2008
Accepted 5 April 2008

PDB Reference: 5′-methylthioadenosine/*S*-adenosylhomocysteine nucleosidase, 3bl6, r3bl6sf.

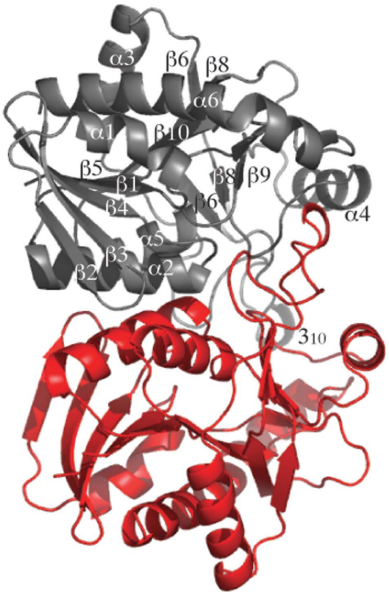

5′-Methylthioadenosine/*S*-adenosylhomocysteine nucleosidase (MTAN) catalyzes the irreversible cleavage of the glycosidic bond in 5′-methylthioadenosine (MTA) and *S*-adenosylhomocysteine (SAH) and plays a key role in four metabolic processes: biological methylation, polyamine biosynthesis, methionine recycling and bacterial quorum sensing. The absence of the nucleosidase in mammalian species has implicated this enzyme as a target for antimicrobial drug design. MTAN from the pathogenic bacterium *Staphylococcus aureus* (*Sa*MTAN) has been kinetically characterized and its structure has been determined in complex with the transition-state analogue formycin A (FMA) at 1.7 Å resolution. A comparison of the *Sa*MTAN–FMA complex with available *Escherichia coli* MTAN structures shows strong conservation of the overall structure and in particular of the active site. The presence of an extra water molecule, which forms a hydrogen bond to the O4′ atom of formycin A in the active site of *Sa*MTAN, produces electron withdrawal from the ribosyl group and may explain the lower catalytic efficiency that *Sa*MTAN exhibits when metabolizing MTA and SAH relative to the *E. coli* enzyme. The implications of this structure for broad-based antibiotic design are discussed.

1. Introduction

5′-Methylthioadenosine/*S*-adenosylhomocysteine nucleosidase (MTAN) is a dual substrate-specific enzyme that irreversibly hydrolyzes the glycosidic bond of 5′-methylthioadenosine (MTA) or *S*-adenosylhomocysteine (SAH) to form adenine and 5′-methylthioribose or *S*-ribosylhomocysteine, respectively (Duerre, 1962). The nucleosidase has been identified as an exploitable antibiotic target because it is essential for the metabolism of MTA and SAH in many microbes such as *Staphylococcus aureus*, *Streptococcus pneumoniae*, *Haemophilus influenzae*, *Mycobacterium tuberculosis* and *Helicobacter pylori* but is not found in mammals. In mammalian systems, the breakdown of MTA and SAH requires two separate enzymes, MTA phosphorylase (Pegg & Williams-Ashman, 1969) and SAH hydrolase (de la Haba & Cantoni, 1959), respectively. Accumulation of MTA and SAH leads to negative-feedback inhibition of four critical metabolic processes: biological methylation (Miller *et al.*, 1994), polyamine biosynthesis (Raina *et al.*, 1982; Pajula & Raina, 1979), methionine recycling (Sufrin *et al.*, 1995; Riscoe *et al.*, 1989) and bacterial quorum sensing (Chen *et al.*, 2002; Schauder *et al.*, 2001).

Eight *Escherichia coli* MTAN structures have been determined (Lee *et al.*, 2001, 2003; Lee, Singh *et al.*, 2005; Lee, Smith *et al.*, 2005) and are available in the Protein Data Bank. These include complexes with substrate and transition-state analogues as well as products and provide a strong foundation for structure-based inhibitor design. The structure of MTAN from the pathogenic bacterium *Streptococcus pneumoniae* has also been determined in complex with a transition-state analogue. To date, two generations of transition-state analogues have been developed and the tightest binding inhibitors exhibit picomolar to femtomolar binding affinity for *E. coli* MTAN (Singh, Evans *et al.*, 2005; Singh, Lee *et al.*, 2005).

To determine whether the structure of the *E. coli* enzyme could be used for broad-based antibiotic design, the structure of the nucleosidase from the pathogenic bacterium *Staphylococcus aureus* (*Sa*MTAN) in complex with the transition-state analogue formycin A

(FMA; Fig. 1) has been determined. This structure provides insight into the inhibitor–enzyme interactions and the mode of nucleoside binding. A comparison of the *Sa*MTAN–FMA and available *E. coli* MTAN structures reveals strong conservation of active-site residues and an identical mode of inhibitor binding. Primary sequence analysis of the enzyme from a number of bacterial pathogens further supports the proposal that any bacterial MTAN structure could serve as a good template for the design of a broad-spectrum antibiotic. However, kinetic characterization demonstrates that knowledge of the structure of the enzyme and the protein–ligand interactions are insufficient to explain the wide range of binding affinities observed for various pathogenic MTANs for a series of transition-state analogues (Gutierrez *et al.*, 2007).

2. Materials and methods

2.1. Protein expression and purification

The *S. aureus pfs* gene was amplified from genomic DNA by the polymerase chain reaction. The gene fragment was subsequently cloned into the *Nde*I and *Xho*I restriction sites of the pET28a vector to allow expression with an N-terminal six-His tag. The plasmid DNA was transformed into BL21 (DE3) cells. Single colonies were picked and grown overnight at 310 K in 50 ml Luria–Bertani broth (LB) containing 100 µ*M* kanamycin. The overnight culture was used to inoculate 1.6 l LB containing a final concentration of 100 µ*M* kanamycin and grown to an OD_{600} of 0.6 at 310 K. Cells were induced by the addition of isopropyl β-D-1-thiogalactopyranoside (IPTG) to 400 µ*M* and cultured for an additional 3 h at 300 K. The induced culture was harvested by centrifugation at 6000 rev min^{-1} in a JA-10 rotor for 10 min. Cells were resuspended in BugBuster Protein Extraction Reagent (Novagen) and lysed by gentle vortexing for 25 min. The crude lysate was fractionated by centrifugation at 18 000 rev min^{-1} in a JA-20 rotor at 277 K for 20 min. The soluble fraction was applied onto a 10 ml FPLC column of Ni–NTA Superflow resin (Qiagen) pre-equilibrated with 25 m*M* potassium phosphate pH 7.5, 250 m*M* NaCl and 20 m*M* imidazole (buffer *A*). The column was washed with three column volumes of buffer *A* and two column volumes of buffer *A* with 150 m*M* imidazole. The recombinant nucleosidase was eluted from the Ni–NTA column with a gradient of buffer *A* plus 150–500 m*M* imidazole. Fractions containing the nucleosidase were dialyzed against 50 m*M* potassium phosphate pH 7.5 overnight at 277 K. Trypsin digestion at 1:1000 dilution for 30 min at room temperature removed the polyhistidine tag, leaving a four-residue (GSHM) linker sequence. The proteolytic reaction was stopped by the addition of polymethylsulfonyl fluoride (PMSF) to a final concentration of 1 m*M*. The nucleosidase was further purified on a Superdex-200 HR 10/30 column pre-equilibrated with 25 m*M* sodium HEPES pH 7.5. Isocratically eluted fractions containing the nucleosidase were pooled and concentrated to 15 mg ml^{-1} using a Millipore BioMax 10K Ultrafree 0.5 ml centrifugal concentrator. The purity and integrity of the sample were checked by SDS–PAGE and electrospray ionization mass spectrometry (Advanced Protein Technology Centre, The Hospital for Sick Children) prior to crystallization studies.

2.2. Kinetic characterization

The catalytic activity of *Sa*MTAN was examined using a xanthine oxidase-coupled spectrophotometric assay (Dunn & Bryant, 1994). For each molecule of adenine oxidized by xanthine oxidase, two molecules of 2-(4-iodophenyl)-3-(4-nitrophenyl)-5-phenyltetrazolium chloride (INT) are reduced to formazan, which absorbs at 470 nm (de Groot *et al.*, 1985). Changes in absorption at 470 nm were converted to the amount of adenine released using a molar absorption coefficient of 15 400 M^{-1} cm^{-1} at pH 7.0. All reactions were performed in 50 m*M* potassium phosphate pH 7.0 using 0.72–4.9 µg *Ec*MTAN or *Sa*MTAN, 0.28 units of xanthine oxidase (Sigma–Aldrich Chemicals) and 1 m*M* INT (Sigma–Aldrich Chemicals) in a final volume of 800 µl. The concentrations of MTA and SAH were varied from 0.31 to 25 µ*M*. The reactions were monitored on a Biochrome Ultrospec 2100 UV–Vis spectrophotometer fitted with the *SWIFT II* enzyme-kinetics software (Amersham Pharmacia Biotech). K_m and V_{max} values were determined by fitting the initial velocity data to the Michaelis–Menten equation using the *SigmaPlot Enzyme Kinetics* module.

2.3. Crystallization

Although a variety of different commercial crystallization screens were tested, the best initial condition for apo-*Sa*MTAN was obtained by the hanging-drop vapour-diffusion technique using Hampton Crystal Screen and contained 100 m*M* sodium HEPES pH 7.5, 0.8 *M* sodium phosphate and 0.8 *M* potassium phosphate. Grid screening was subsequently performed to optimize the buffer and precipitant concentrations. The best quality crystals were obtained using 50 m*M* potassium phosphate with 20%(*w*/*v*) PEG 8000. The crystals of *Sa*MTAN–FMA were prepared by first pre-incubating the protein with 1 m*M* formycin A for 2 h on ice. Crystals with approximate dimensions of 0.2 × 0.2 × 0.2 mm grew within one week.

2.4. Data collection and processing

In preparation for data collection at liquid-nitrogen temperatures, the *Sa*MTAN–FMA crystal was soaked for 2 min in a cryoprotectant [20%(*w*/*v*) PEG 8000, 50 m*M* potassium phosphate, 1.5 m*M* formycin A and 15%(*v*/*v*) glycerol] prior to flash-freezing in the cryostream.

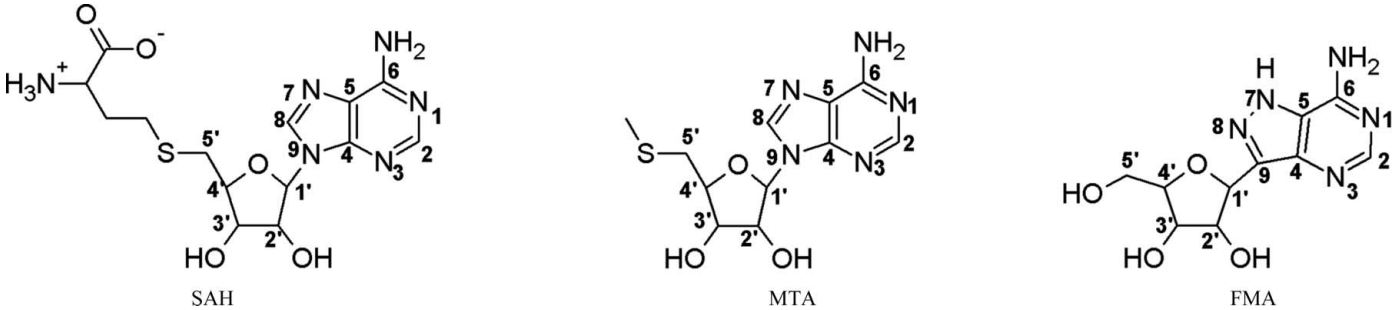

Figure 1
Structures of SAH, MTA and FMA. Note that for ease of comparison, the numbering of atoms in the purine base of the inhibitor FMA is based on the numbering convention of MTA and not the IUPAC standard.

Data were measured on an R-AXIS IV^{++} image plate using an RUH3R rotating copper-anode X-ray generator with Osmic optics at The Hospital for Sick Children. The data were indexed, integrated, scaled and merged using *d*TREK* (Pflugrath, 1999).

2.5. Structural determination and refinement

The structure of *Sa*MTAN–FMA was determined by molecular replacement using only the protein coordinates of the structure of *E. coli* MTAN complexed with FMA (*Ec*MTAN–FMA) as the search model (PDB code 1nc3). *CNS-SOLVE* was used for all structure-determination and refinement steps (Brünger *et al.*, 1998). Data between 15 and 4 Å resolution were included in the cross-rotation and translation functions and produced an $R_{\rm cryst}$ of 46.6%. The resulting model was subjected to an initial round of rigid-body refinement and maximum-likelihood torsion-angle refinement (Brünger *et al.*, 1998) prior to replacing the *E. coli* sequence with the *S. aureus* sequence. Rounds of manual rebuilding using *Xfit* (McRee, 1999) were subsequently alternated with maximum-likelihood torsion-angle refinement starting at 5000 K using all data, a bulk-solvent correction and an anisotropic *B*-factor correction. The progress of the refinement was monitored by reductions in $R_{\rm cryst}$ and $R_{\rm free}$ and $\sigma_{\rm A}$-weighted $2F_{\rm o} - F_{\rm c}$ and $F_{\rm o} - F_{\rm c}$ maps as implemented in *CNS* (Read, 1986) were carefully examined at the end of each round of refinement. A $\sigma_{\rm A}$-weighted $F_{\rm o} - F_{\rm c}$ map calculated after the initial round of torsion-angle refinement revealed strong positive electron density corresponding to formycin A in the *Sa*MTAN active site. The FMA coordinates were obtained from the *Ec*MTAN–FMA structure

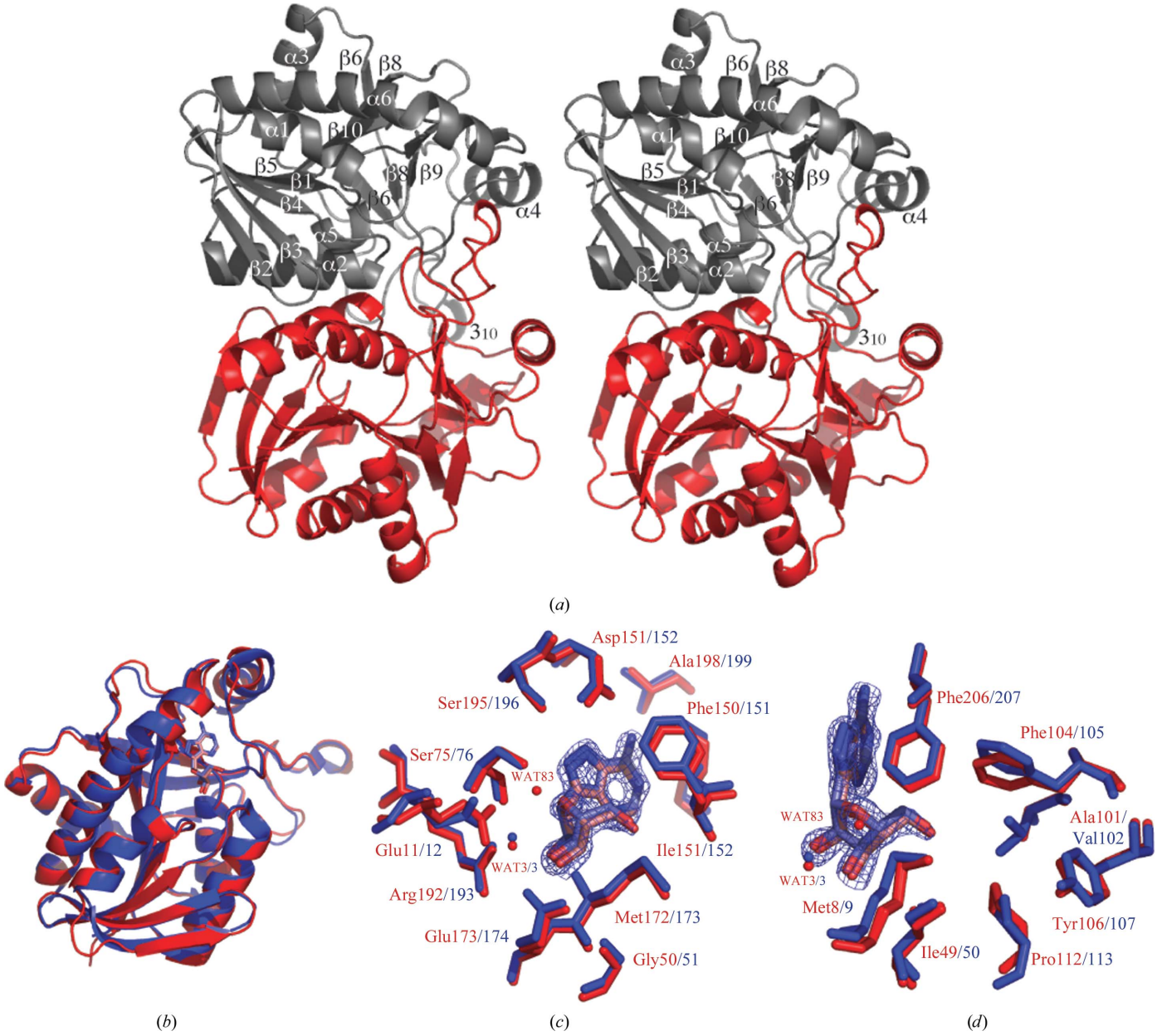

Figure 2
Structure of *Sa*MTAN and a comparison to *Ec*MTAN. (*a*) Stereo diagram of the quaternary structure of *Sa*MTAN. Superpositions of (*b*) the monomeric structures, (*c*) the adenine and ribose subsites and (*d*) the 5-alkythio-binding subsites of *Sa*MTAN–FMA (red) and *Ec*MTAN–FMA (blue). The initial $\sigma_{\rm A}$-weighted $F_{\rm o} - F_{\rm c}$ electron-density map found in the *Sa*MTAN–FMA structure is shown contoured at 3σ with the refined coordinates of the protein and ligand. This figure was generated using *PyMOL* (DeLano, 2002).

and topology and parameter files were generated using the *XPLO2D* server (Kleywegt, 1995). Water molecules were added during the later rounds of refinement in accord with good electron density (σ_A-weighted $F_o - F_c$ peaks greater than 3σ) and the formation of hydrogen bonds (less than 3.2 Å) or van der Waals contacts less than 4.0 Å to other atoms. After the addition of the inhibitor and water molecules, alternating rounds of conjugate-gradient refinement and model rebuilding using *Xfit* were performed followed by individual isotropic *B*-factor refinement. In the final refined structure of *Sa*MTAN–FMA, all 228 protein residues and two of the four residues from the N-terminal tag were modelled. Analysis of the structure using *MOLPROBITY* (Lovell *et al.*, 2003) showed that more than 97% of residues are in the favoured regions and 100% of residues are in the allowed regions of the Ramachandran plot. Data-collection and refinement statistics are reported in Table 1. In the following subsequent analyses, the structure of *Sa*MTAN–FMA was aligned with *Ec*MTAN–FMA (PDB code 1nc3) and with the *E. coli* enzyme complexed with adenine (ADE; *Ec*MTAN–ADE; PDB code 1jys) by a nonlinear least-squares fit of all main-chain (N—C^{α}—C) atoms using the program *PROFIT* (Smith, 1993).

Table 1
Data-collection and refinement statistics for *Sa*MTAN–FMA.

Values in parentheses are for the last resolution shell.

Space group	$P2_12_12$
Unit-cell parameters (Å)	a = 58.25, b = 81.67, c = 45.46
Resolution (Å)	32.8–1.70 (1.76–1.70)
R_{merge}† (%)	2.8 (11.0)
No. of measured reflections	137412
No. of unique reflections	24529
Redundancy	5.5
Completeness (%)	93.1 (88.1)
Average $I/\sigma(I)$	19.9 (5.8)
R_{cryst}‡	18.2 (26.6)
R_{free}‡	18.7 (29.7)
No. of protein atoms	1718
No. of waters	192
No. of ligand atoms	19
R.m.s.d. bonds (Å)	0.010
R.m.s.d. angles (°)	1.4
R.m.s.d. dihedrals (°)	23.8
Average *B* factor (Å^2)	
Protein	12.5
Ligand	8.5
Water	23.7
Ramachandran plot§ (%)	
Favoured	97
Allowed	3
Cross-validated σ_A coordinate error (Å)	0.14

† $R_{merge} = \sum_{hkl}\sum_i |I_i(hkl) - \langle I(hkl)\rangle| / \sum_{hkl}\sum_i I_i(hkl)$, where $I_i(hkl)$ is the measured intensity for each symmetry-related reflection and $\langle I(hkl)\rangle$ is the mean intensity for the unique reflection. ‡ $R_{cryst} = \sum ||F_o| - k|F_c|| / \sum |F_o|$ and $R_{free} = \sum ||F_{os}| - k|F_{cs}|| / \sum |F_{os}|$, where 's' refers to a subset of data not used in the refinement that represents 5% of the total number of observations (1110 reflections). § As calculated using *MOLPROBITY* (Lovell *et al.*, 2003).

3. Results and discussion

3.1. Kinetic characterization

*Sa*MTAN has comparable binding affinities but reduced maximum velocities for the substrates MTA and SAH compared with *Ec*MTAN (Table 2). The maximum velocities for *Sa*MTAN for MTA and SAH are reduced 52-fold and 53-fold, respectively. The catalytic efficiency of *Sa*MTAN towards MTA and SAH is approximately ninefold and 25-fold lower, respectively, than that of *Ec*MTAN. The reduced catalytic efficiency of *Sa*MTAN may be rationalized by a structural difference in the active site, as described below.

3.2. Structural determination and comparison of MTANs

3.2.1. Overall structure. *Sa*MTAN crystallizes with a monomer in the asymmetric unit. Each monomer consists of a mixed α/β domain, with a central mixed ten-stranded β-sheet flanked by six α-helices and a small 3_{10}-helix (Fig. 2*a*). The biologically active dimer is generated by the action of a crystallographic twofold axis (residues from the α2, α5, α6 and 3_{10} helices and th,e loops between β2 and β3 and between β4 and α2). The interface area between the two monomers is 1506.3 Å^2 and comprises 15% of the surface of each monomer (Krissinel & Henrick, 2007).

*Ec*MTAN has previously been shown to exist in two different conformations: 'open' and 'closed' (Lee *et al.*, 2001, 2003). The 'open' state is defined by a larger and more solvent-accessible purine- and ribose-binding site, as seen in the adenine (*Ec*MTAN–ADE; Lee *et al.*, 2001) and glycerol complexes (*Ec*MTAN–GOL; Lee, Smith *et al.*, 2005). Structures of *E. coli* enzyme–inhibitor complexes suggest that substrate binding induces a series of conformational changes to a 'closed' state (Lee *et al.*, 2003). In the 'closed' state, all water molecules except for the catalytic water are excluded from the active site. For the purposes of the following discussion, we have selected the *Ec*MTAN–FMA (Lee *et al.*, 2003) and *Ec*MTAN–ADE (Lee *et al.*, 2001) structures as the representative *E. coli* structures for the 'closed' and 'open' conformations, respectively. A comparison of *Sa*MTAN–FMA with the *Ec*MTAN–FMA and *Ec*MTAN–ADE structures reveals C^{α} root-mean-square displacements of 0.55 and 1.37 Å, respectively, showing that the overall structure of *Sa*MTAN–FMA is more similar to the ligand-induced 'closed' conformation of *Ec*MTAN than the 'open' conformation.

3.2.2. Active site. The nucleosidase active site is typically described in terms of three subsites that accommodate the adenine, ribose and 5′-alkylthio moieties of the substrate. The initial σ_A-weighted $F_o - F_c$ map revealed strong electron density corresponding to the inhibitor formycin A in the active site (Figs. 2*c* and 2*d*). Note that the amino-acid sequence in *Sa*MTAN is shifted by −1 relative to the numbering of the *E. coli* homologue. In the purine-binding subsite (Fig. 3*a*), $O^{\delta1}$ and $O^{\delta2}$ of Asp196 make hydrogen bonds to the N_6 and N_7 atoms of the purine base of formycin A, respectively. Asp196 is stabilized by two hydrogen bonds from Ser195 O^{γ} and the amide N atom of Ala198. The purine N_6 and N_1 atoms also form hydrogen bonds to the main-chain carbonyl O atom and amide N atom of Ile152, respectively. Phe150 makes a base-stacking interaction with the purine ring. A hydrogen bond (3.0 Å) exists between Ser75 O^{γ} and the purine N_8 atom. Residues Glu11, Ser75, Met172 and Glu173 lie on the surface of the ribose-binding subsite, while two water molecules are found within this subsite. The ribose is anchored by van der Waals interactions between the side chain of Met172 and the hydrophobic face of the ribose and by a hydrogen bond between the amide N atom of Met172 and the 2′-hydroxyl. In addition, the ribosyl 2′- and 3′-hydroxyl O atoms donate protons to the $O^{\varepsilon1}$ and $O^{\varepsilon2}$ carboxylate groups of Glu173. Two water molecules (WAT3 and WAT83) interact with the ribose moiety. As in the *E. coli* MTAN structures, WAT3 is the putative nucleophilic water molecule. This water molecule is approximately 3.6 Å from the anomeric carbon and forms hydrogen bonds to the ribosyl 3′-hydroxyl O atom (2.7 Å), Glu11 $O^{\varepsilon2}$ (2.7 Å) and Arg192 $N^{\eta1}$ (2.9 Å). WAT83 forms a 2.8 Å hydrogen bond to the ribosyl $O_{4'}$ ring O atom and 2.6 and 3.0 Å hydrogen bonds to Glu11 $O^{\varepsilon2}$ and Ser75 O^{γ}, respectively. The 5′-substituent of formycin A makes intrasubunit van der Waals interactions with residues Met8, Ile49, Phe150, Met172 and Phe206 and intersubunit van der Waals interactions with Phe104 and Pro112. Residues Ala101 and Tyr106 also form the 5′-alkylthio-binding site but do not make any van der

Table 2
Kinetic parameters for *Sa*MTAN and *Ec*MTAN.

	*Sa*MTAN		*Ec*MTAN	
	MTA	SAH	MTA	SAH
V_{max} (μmol min^{-1} mg^{-1})	(1.17 ± 0.03) × 10^{-2}	(1.05 ± 0.04) × 10^{-2}	0.61 ± 0.04	0.55 ± 0.06
K_m (μ*M*)	1.24 ± 0.14	2.52 ± 0.36	7.38 ± 1.16	5.30 ± 1.22
k_{cat} (s^{-1})	(9.73 ± 0.24) × 10^{-3}	(8.73 ± 0.36) × 10^{-3}	0.49 ± 0.03	0.45 ± 0.05
k_{cat}/K_m (*M*$^{-1}$ s^{-1})	(7.82 ± 0.89) × 10^{3}	(3.46 ± 0.51) × 10^{3}	(6.69 ± 1.15) × 10^{4}	(8.48 ± 2.13) × 10^{4}

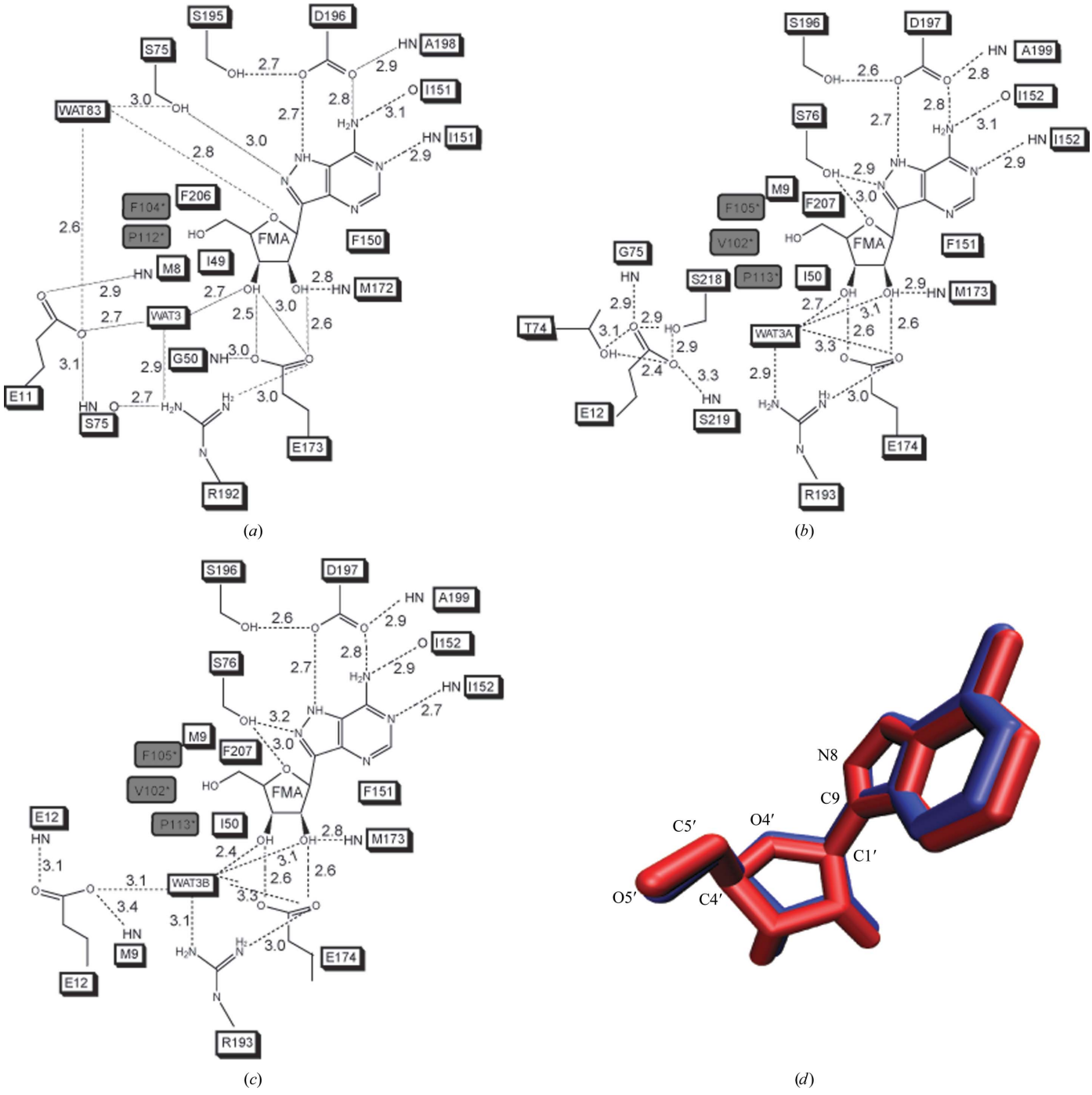

Figure 3
Inhibitor conformation and interactions. Schematics of the interactions between the ligand and the protein in the active sites of (*a*) *Sa*MTAN–FMA, (*b*) monomer *A* of *Ec*MTAN–FMA and (*c*) monomer *B* of *Ec*MTAN–FMA. Residues donated by a neighbouring subunit are shaded in a grey box and marked with an asterisk. Dotted lines represent protein–protein, protein–ligand or protein–solvent hydrogen bonds, with distances given in angstroms. (*b*) and (*c*) are modified from Lee *et al.* (2003) and Lee *et al.* (2001). (*d*) Superposition of formycin A from the active sites of the *S. aureus* (red) and *E. coli* (blue) enyzmes. The figure was generated using *VMD* (Humphrey *et al.*, 1996).

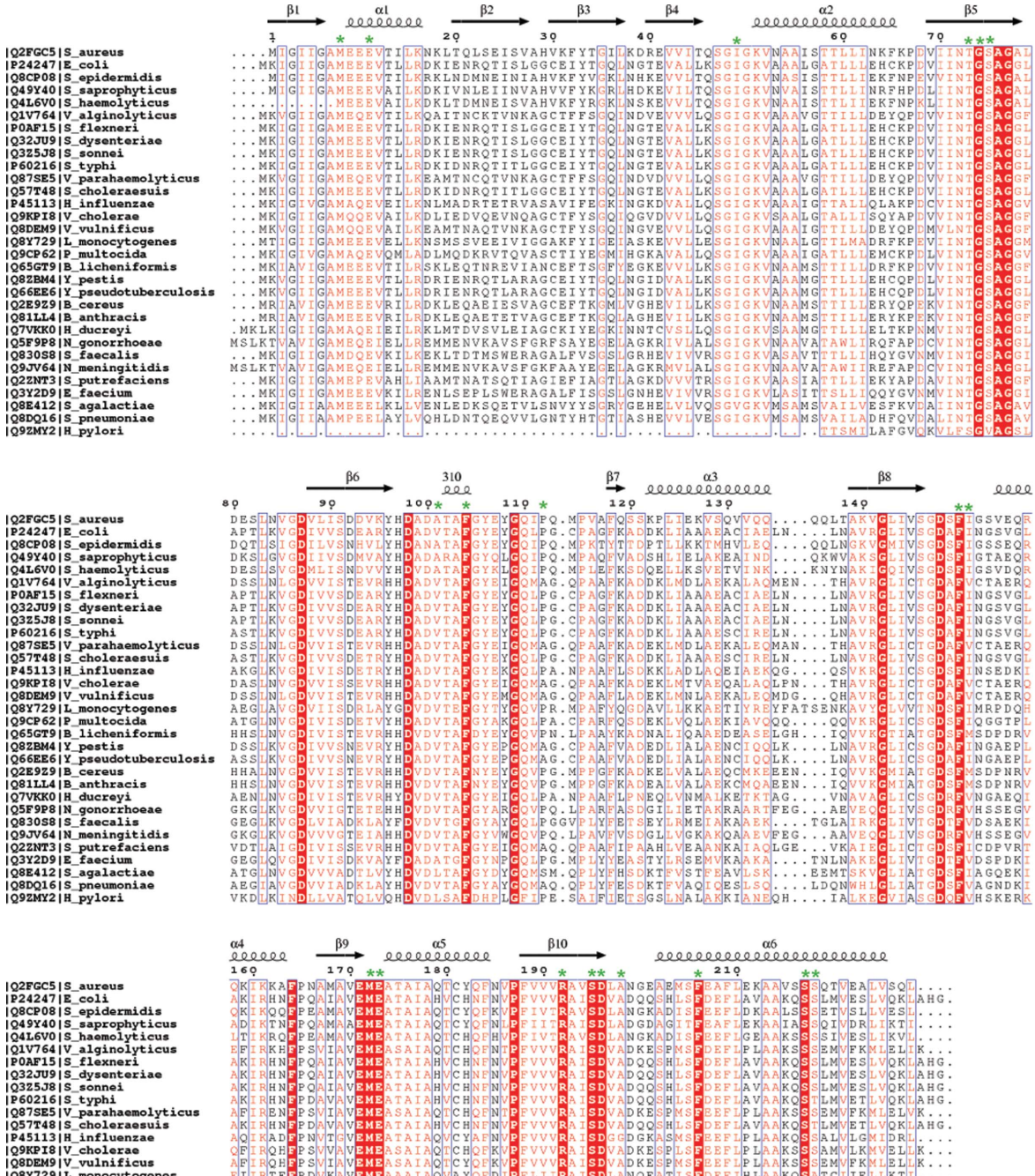

Figure 4
Sequence alignment of *E. coli* and selected pathogenic MTA/SAH nucleosidases. The primary sequences of MTAN from the following bacterial pathogens are aligned: *Staphylococcus aureus*, *Escherichia coli*, *Staphylococcus epidermidis*, *Staphylococcus saprophyticus*, *Staphyloccocus haemolyticus*, *Vibrio alginoyticus*, *Shigella flexneri*, *Shigella dysenteriae*, *Shigella sonnei*, *Salmonella typhi*, *Vibrio parahaemolyticus*, *Salmonella choleraesuis*, *Haemophilus influenzae*, *Vibrio cholerae*, *Vibrio vulnificus*, *Listeria monocytogenes*, *Pasteurella multocida*, *Bacillus licheniformis*, *Yersina pestis*, *Yersinia pseudotuberculosis*, *Bacillus cereus*, *Bacillus anthracis*, *Haemophilus ducreyi*, *Neisseria gonorrhoeae*, *Streptococcus faecalis*, *Neisseria meningitides*, *Shewanella putrefaciens*, *Enterococcus faecium*, *Streptococcus agalactiae*, *Streptococcus pneumoniae* and *Helicobacter pylori*. The sequence numbering and secondary-structural elements are based on *Staphylococcus aureus*. Residues that are strictly conserved are displayed as white characters in a red box, while residues that have been conservatively substituted are displayed as red characters. Residues that are similar across groups are framed in blue. Residues in the active site are marked with a green asterisk. This figure was prepared using *ESPript* (Gouet *et al.*, 1999). The multiple sequence alignment was generated using *ClustalW* (Combet *et al.*, 2000).

Waals interactions to the ligand. The 5′ hydroxyl of formycin A makes no hydrogen bonds to the protein. The longer 5′-methylthio or homocysteinyl groups in the natural substrates, MTA and SAH, would be likely to interact with Ala101 and Tyr106.

A comparison of the active-site architectures of *S. aureus* MTAN and *E. coli* MTAN reveals a striking similarity (Figs. 2*c*, 2*d* and 3). The positions of the putative catalytic acid (Asp197/Asp196), catalytic base (Glu12/Glu11) and nucleophilic water (WAT3) are all conserved. In addition, all of the residues involved in substrate binding are conserved, with the exception of Val102, which is replaced by Ala101 in *Sa*MTAN (Fig. 2*d*). This conservative substitution does not appear to perturb the architecture of the binding site or the specificity of the enzyme. The average displacement of the C^{α} positions of residues in the active site is 0.3 Å and the side-chain conformations and hydrogen-bond distances are nearly identical. The only significant difference is the presence of an extra water molecule (WAT83) in the *S. aureus* enzyme, which forms hydrogen bonds to Ser75, Glu11 and the $O_{4'}$ atom of the ligand. This additional hydrogen bond to $O_{4'}$ of the ligand would cause electron withdrawal from the ribosyl group and from the $\sigma^*(C_{1'}-N_9)$ antibonding orbital, thereby strengthening the $C_{1'}-N_9$ covalent bond. This is likely to contribute to the reduction in catalytic efficiency in *Sa*MTAN compared with *Ec*MTAN. While WAT83 is absent from all available inhibitor-complexed structures of *Ec*MTAN, this second water molecule is also present in the 1.6 Å ligand-bound structure of *Streptococcus pneumoniae* MTAN (PDB code 1zos). Like *Sa*MTAN, *S. pneumoniae* MTAN is also less catalytically efficient compared with *E. coli* MTAN (Singh & Schramm, 2007). In the structures of *Sa*MTAN and *S. pneumoniae* MTAN, the side chains of Met8/9 are directed away from WAT83. In *Ec*MTAN Met9 C^{ξ} occupies the place where WAT83 would be, hence explaining the displacement of WAT83 from the *Ec*MTAN active site.

3.2.3. Nucleoside conformations and implications for the catalytic mechanism. In solution, MTA and SAH are found predominantly in the *anti* conformation with a ribosidic torsion angle ($C_8-N_9-C_{1'}-O_{4'}$) of 45° (Markham *et al.*, 2002). The binding of nucleosides to MTAN has previously been shown to significantly alter the conformation of the nucleoside. In the *Sa*MTAN–FMA structure, formycin A adopts a highly *anti* $N_9-C_{1'}$ ribosidic bond conformation and a high-energy $C_{4'}$-*endo* sugar pucker. These energetically unfavourable conformations are likely to place strain on the ribosidic $N_9-C_{1'}$ bond and facilitate cleavage. The exocyclic $C_{4'}-C_{5'}$ bond can be described by two torsion angles, φ_{oo} ($O_5-C_{5'}-C_{4'}-O_{4'}$) and φ_{oc} ($O_5-C_{5'}-C_{4'}-C_{3'}$). In the *Sa*MTAN–FMA structure, $\varphi_{oo} = -179.6°$ and $\varphi_{o} = -68.3°$, corresponding to a *trans*, *gauche* conformation. Superposition of formycin A from *S. aureus* and *E. coli* reveal identical nucleoside conformations (Fig. 3*d*). Given that the overall structure, active-site residues and ligand-binding interactions are conserved between the *E. coli* and *S. aureus* enzymes, we anticipate that the catalytic mechanism will be the same. This conclusion is supported by the recent studies of the transition-state structure of various MTANs (Gutierrez *et al.*, 2007). Both the *S. aureus* and *E. coli* enzymes were found to exhibit a late dissociative transition state.

3.3. Implications for structure-based drug design

The structure of *S. aureus* MTAN establishes that the architecture of its active site and the nucleoside–enzyme interactions are identical to those found in the *E. coli* enzyme. The recently determined structure of the *S. pneumoniae* enzyme also shows structural similarity to the *E. coli* enzyme (Singh *et al.*, 2006). The primary sequence alignment of MTANs from multiple bacterial pathogens demonstrates sequence identity of between 30% and 100% (Fig. 4), with almost all active-site residues being conserved. The observed structural similarity suggests that any of the available structures could be used for modelling or docking studies for the design of broad-spectrum antibiotics, where the dynamics of the protein are ignored. As the ninefold to 25-fold decrease in catalytic efficiency observed for the *S. aureus* enzyme relative to the *E. coli* enzyme (Table 2) does not fully explain the 700-fold to 1000-fold differences observed in the binding affinities of the methylthio-ImmA and methylthio-DADMe-ImmA transition-state analogues (7.7×10^4 *versus* 77 p*M* for ImmA and 1.4×10^3 *versus* 2 p*M* for DADMe-ImmA, respectively; Gutierrez *et al.*, 2007), inhibitor design for MTAN and the potency of an inhibitor for a particular bacterial species needs to consider not only the catalytic efficiency of the individual enzyme but also its dynamics. The structure of the *Sa*MTAN–FMA complex presented here clearly shows that structural data alone are insufficient to explain the wide range of binding affinities found for various transition-state analogues (Gutierrez *et al.*, 2007) as the protein–ligand interactions observed in the crystal structures are comparable in almost all cases.

The authors thank Dr Feher and Dr Appelt for providing the expression vector for the *Sa*MTAN, Dr Yuri Lobsanov for his help with data collection and Dr Yi-Min Shi and Li Zhang at the Advanced Protein Technology Centre (APTC) at The Hospital for Sick Children for their assistance with the mass spectrometry. This work was supported by an operating grant from the Canadian Institutes of Health Research (#43998) and a sponsored research agreement from Quorex Pharmaceuticals. PLH is the recipient of a Canada Research Chair; JEL was supported, fully or in part, by a Graduate Doctoral training award from CIHR and a studentship from the Ontario Student Opportunities Trust Fund and Hospital for Sick Children Foundation Student Scholarship Program; KKWS was supported, fully or in part, by a Master's research award from the Natural Science and Engineering Research Council of Canada, a studentship from the Ontario Student Opportunities Trust Fund and Hospital for Sick Children Foundation Student Scholarship Program and a Canada Graduate scholarship from CIHR.

References

Brünger, A. T., Adams, P. D., Clore, G. M., DeLano, W. L., Gros, P., Grosse-Kunstleve, R. W., Jiang, J.-S., Kuszewski, J., Nilges, M., Pannu, N. S., Read, R. J., Rice, L. M., Simonson, T. & Warren, G. L. (1998). *Acta Cryst.* D**54**, 905–921.
Chen, X., Schauder, S., Potier, N., Van Dorsselaer, A., Pelczer, I., Bassler, B. L. & Hughson, F. M. (2002). *Nature (London)*, **415**, 545–549.
Combet, C., Blanchet, C., Geourjon, C. & Deléage, G. (2000). *Trends Biochem. Sci.* **25**, 147–150.
DeLano, W. L. (2002). *The PyMOL Molecular Graphics System.* http://www.pymol.org.
Duerre, J. A. (1962). *J. Biol. Chem.* **237**, 3737–3741.
Dunn, S. & Bryant, J. (1994). *Phytochem. Anal.* **5**, 286–293.
Gouet, P., Courcelle, E., Stuart, D. I. & Metoz, F. (1999). *Bioinformatics*, **15**, 305–308.
Groot, H. de, de Groot, H. & Noll, T. (1985). *Biochem. J.* **230**, 255–260.
Gutierrez, J. A., Luo, M., Singh, V., Li, L., Brown, R. L., Norris, G. E., Evans, G. B., Furneaux, R. H., Tyler, P. C., Painter, G. F., Lenz, D. H. & Schramm, V. L. (2007). *ACS Chem. Biol.* **2**, 725–734.
Haba, G. de la & Cantoni, G. (1959). *J. Biol. Chem.* **234**, 603–608.
Humphrey, W., Dalke, A. & Schulten, K. (1996). *J. Mol. Graph.* **14**, 33–38.
Kleywegt, G. (1995). *Jnt CCP4/ESF–EACBM Newsl. Protein Crystallogr.* **31**, 45–50.
Krissinel, E. & Henrick, K. (2007). *J. Mol. Biol.* **372**, 774–797.
Lee, J. E., Cornell, K. A., Riscoe, M. K. & Howell, P. L. (2001). *Structure*, **9**, 941–953.

Lee, J. E., Cornell, K. A., Riscoe, M. K. & Howell, P. L. (2003). *J. Biol. Chem.* **278**, 8761–8770.
Lee, J. E., Singh, V., Evans, G. B., Tyler, P. C., Furneaux, R. H., Cornell, K. A., Riscoe, M. K., Schramm, V. L. & Howell, P. L. (2005). *J. Biol. Chem.* **280**, 18274–18282.
Lee, J. E., Smith, G. D., Horvatin, C., Huang, D. J., Cornell, K. A., Riscoe, M. K. & Howell, P. L. (2005). *J. Mol. Biol.* **352**, 559–574.
Lovell, S. C., Davis, I. W., Arendall, W. B. III, de Bakker, P. I., Word, J. M., Prisant, M. G., Richardson, J. S. & Richardson, D. C. (2003). *Proteins*, **50**, 437–450.
McRee, D. E. (1999). *J. Struct. Biol.* **125**, 156–165.
Markham, G. D., Norrby, P. O. & Bock, C. W. (2002). *Biochemistry*, **41**, 7636–7646.
Miller, J. W., Nadeau, M. R., Smith, J., Smith, D. & Selhub, J. (1994). *Biochem. J.* **298**, 415–419.
Pajula, R. L. & Raina, A. (1979). *FEBS Lett.* **99**, 343–345.
Pegg, A. E. & Williams-Ashman, H. G. (1969). *J. Biol. Chem.* **244**, 682–693.
Pflugrath, J. W. (1999). *Acta Cryst.* D**55**, 1718–1725.
Raina, A., Tuomi, K. & Pajula, R. L. (1982). *Biochem. J.* **204**, 697–703.
Read, R. J. (1986). *Acta Cryst.* A**42**, 140–149.
Riscoe, M. K., Ferro, A. J. & Fitchen, J. H. (1989). *Parasitol. Today*, **5**, 330–333.
Schauder, S., Shokat, K., Surette, M. G. & Bassler, B. L. (2001). *Mol. Microbiol.* **41**, 463–476.
Singh, V., Evans, G. B., Lenz, D. H., Mason, J. M., Clinch, K., Mee, S., Painter, G. F., Tyler, P. C., Furneaux, R. H., Lee, J. E., Howell, P. L. & Schramm, V. L. (2005). *J. Biol. Chem.* **280**, 18265–18273.
Singh, V., Lee, J. E., Nunez, S., Howell, P. L. & Schramm, V. L. (2005). *Biochemistry*, **44**, 11647–11659.
Singh, V. & Schramm, V. L. (2007). *J. Am. Chem. Soc.* **129**, 2783–2795.
Singh, V., Shi, W., Almo, S. C., Evans, G. B., Furneaux, R. H., Tyler, P. C., Painter, G. F., Lenz, D. H., Mee, S., Zheng, R. & Schramm, V. L. (2006). *Biochemistry*, **45**, 12929–12941.
Smith, G. (1993). *PROFIT: A Program for Orienting One Protein Molecule Onto Another by a Least Squares Procedure.* Hauptman–Woodward Medical Research Institute, Buffalo, USA.
Sufrin, J. R., Meshnick, S. R., Spiess, A. J., Garofalo-Hannan, J., Pan, X. Q. & Bacchi, C. J. (1995). *Antimicrob. Agents Chemother.* **39**, 2511–2515.